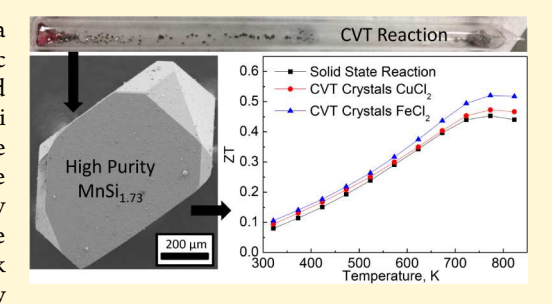


Thermoelectric Properties of Undoped High Purity Higher Manganese Silicides Grown by Chemical Vapor Transport

Steven N. Girard, *, Xi Chen, * Fei Meng, * Ankit Pokhrel, * Jianshi Zhou, * Li Shi, * and Song Jin*, *

Supporting Information

ABSTRACT: Semiconducting higher manganese silicides (HMS), with a nominal composition of MnSi_{1.73}, are particularly promising thermoelectric materials because of their elemental abundance, nontoxicity, and reported ZT of around 0.4 at 800 K for undoped samples. However, embedded MnSi impurities naturally form during the melt growth of HMS materials. The influences of such naturally occurring MnSi impurities within bulk HMS have yet to be carefully studied. Herein, we report the synthesis of high-purity MnSi-free single crystals of HMS by chemical vapor transport and the thermoelectric properties of consolidated HMS samples prepared by spark plasma sintering (SPS). The high purity of the HMS crystals is verified by



scanning and transmission electron microscopy, electron diffraction, and synchrotron high-resolution X-ray diffraction. Despite successfully growing high purity HMS single crystals, we find that MnSi will nevertheless precipitate from HMS after SPS processing. In-situ sychrotron high-resolution X-ray diffraction experiments show that HMS are unstable at high temperatures. Despite the precipitation of MnSi inclusions within the HMS materials, we show that samples prepared from undoped single crystals of HMS exhibit higher hole mobilities owing to their higher purity, resulting in an improved maximum ZT of 0.52 ± 0.08 at 750 K.

■ INTRODUCTION

Thermoelectric heat-to-power generation may serve an important role in renewable energy production by recouping the heat wasted in many industrial, transportation, commercial, and residential processes, such as wasted heat as a byproduct of the combustion of fossil fuels in automobiles and industrial power plants. 1-4 However, thermoelectric materials have yet to reach wide-scale utilization, due to their typical combination of low efficiencies and high material cost. The thermoelectric efficiency is related to the thermoelectric figure of merit ZT, defined as $ZT = \sigma S^2 T / \kappa_{tot}$, where σ is the electrical conductivity, S is the Seebeck coefficient, T is the operating temperature, and $\kappa_{\rm tot}$ is the total thermal conductivity. The wide-scale utilization of thermoelectric materials for waste heat-to-power conversion will depend both on high ZT as well as materials comprised of primarily low-cost and preferably nontoxic elements. Many current state-of-the-art thermoelectric materials contain toxic (Pb, Tl)⁵⁻⁷ and expensive and rare elements (Te, Ge, and Sb). 8-10 In this regard, semiconducting silicide thermoelectric materials are attractive because they are low-cost, nontoxic, can operate at temperatures >1000 K, and are extremely chemically robust and inert.11

A number of narrow-band gap semiconducting silicides have been discovered, including Mg₂Si, ¹² FeSi₂, ¹³ CrSi₂, ¹⁴ MnSi_{1.73}, ¹⁵ ReSi_{1.75}, ¹⁶ and Ru₂Si₃. ^{17,18} Of these, MnSi_{1.73}, higher manganese silicides (or HMS), are particularly interesting for thermoelectric applications owing to their complex crystal structures

and promising thermoelectric properties. HMS are a series of homologous compounds known as Nowotny Chimney-Ladder (NCL) phases with the general structure Mn_nSi_{2n-m} , where n =4, 7, 11, 15, 19, 23, 26, 27, 39, with the corresponding m = 1, 2, 3, 4, 5, 6, 7, and 10, respectively. ^{19–22} It has been suggested that the structural complexity of HMS is responsible for its rather low and nearly constant values of thermal conductivity of between 2 and 4 W/mK from 300 to 1000 K. This, coupled with high values of power factor $\sim 10 \, \mu \text{W}/(\text{cm K}^2)$, results in reproducible ZT of ~0.4 at 800 K for undoped HMS, which has been corroborated by recent reports.^{23–25} Furthermore, the enhancement in ZT of HMS has been recently reported for systems utilizing Re, Cr, Ge, Al, Si, and Fe dopants or substitutions as a means of enhancing the power factor $S^2\sigma$ and suppressing the lattice thermal conductivity ($\kappa_{\rm lat}$) of HMS. ^{18,26–32} These recent works have reported a maximum ZT of around 0.6 at around 800 K in doped HMS^{25,28-30,33} whereas ZT as high as 0.75 at 800 K was claimed in a so-called complex-doped HMS.18

It is important to note that, in the formation of HMS, either directly from the homogeneous liquid phase or through solidstate diffusion at elevated temperatures, MnSi precipitation occurs due to the peritectic solidification which results in the

Received: July 1, 2014 Revised: August 7, 2014 Published: August 13, 2014

[†]Department of Chemistry, University of Wisconsin—Madison, Madison, Wisconsin 53706, United States

^{*}Materials Science and Engineering Program, Texas Materials Institute, The University of Texas at Austin, Austin, Texas 78712, United States

coexistence of solid MnSi and liquid HMS or by the slow solidstate diffusion of Si which results in inhomogeneous phase formation and stabilization. It has been suggested that intrinsic metallic MnSi impurities that become embedded throughout the HMS matrix as a result of the peritectic phase transformation, as is shown in the Mn-Si phase diagram, could be responsible for limiting thermoelectric efficiency. 15,34 Previous work has showed that, from the melt, MnSi will naturally phase segregate in HMS perpendicular to the c-axis. 15 MnSi is itself a technologically intriguing material within the field of spintronics because of its interesting magnetic properties, 35,36 as well as an excellent contact material. 11 However, MnSi is metallically conducting, with a very large carrier concentration, low Seebeck coefficient, and large thermal conductivity. Because of this, the MnSi impurities within HMS could adversely affect the thermoelectric properties of HMS. 15,33 However, there have been no detailed studies to adequately determine the effects of MnSi on the thermoelectric transport of HMS. What has been lacking is a chemical means to synthesize high purity HMS without MnSi. The phase purity has only been confirmed in discrete nanostructured systems, particularly in HMS nanowires, ^{20,37} but not in bulk HMS samples.

Herein we report the growth and characterization of high purity HMS single crystals and the thermoelectric properties of HMS samples consolidated from HMS single crystals using spark plasma sintering (SPS). Using a chemical vapor transport (CVT) approach, we can grow single crystals of HMS without MnSi impurities. The high phase purity of the HMS crystals is verified using synchrotron X-ray diffraction as well as scanning and transmission electron microscopy. However, we find that the high-purity HMS synthesized in this manner is thermodynamically unstable at high temperature. In situ hightemperature synchrotron studies reveal the precipitation of MnSi around 900 °C, albeit at lower concentrations as compared to bulk HMS samples prepared by conventional solid-state reactions (SSRs). The effect of the smaller MnSi precipitates observed in the CVT samples on the thermoelectric properties is addressed, showing a slight improvement in the maximum ZT from 0.45 ± 0.06 to 0.52 ± 0.08 at 750 K. Our findings suggest that MnSi precipitation is likely difficult or impossible to avoid in bulk HMS materials but at low concentrations is perhaps not as damaging to the thermoelectric properties as previously thought.

■ EXPERIMENTAL SECTION

Growth of HMS Single Crystals. High-purity single crystals of HMS were synthesized by a chemical vapor transport (CVT) method adapted from the report by Kojima et al. 38,39 The HMS starting material was synthesized using a solid state reaction (SSR) by reacting high purity Si (99.999%, Espi Metals) and Mn (99.99%, Kamis) at a ratio of 1.73:1 at 1200 °C in fused silica ampules sealed under a residual vacuum of $\sim \! 10^{-3}$ Torr. We note that at $1200\,\,^{\circ}\text{C}$ there exists a solid-liquid equilibrium of the reactants (via a peritectic solidification), 40 and that in this work we broadly use the term SSR to describe a typical high temperature reaction starting from elemental precursors. To ensure elemental homogeneity, this procedure was repeated twice. For the CVT reactions, ~0.4 g of SSR material was added to a fused silica tube (inner diameter 11 mm and length ~23 cm) with ~40 mg of metal halide transport agent, which was sealed under vacuum and placed in a home-built two-zone furnace. The combined HMS powder and transport agent were placed in the hot zone of the furnace at 1000 °C and allowed to transport to the cold end of the furnace maintained at 800 $^{\circ}$ C, over the course of 2 weeks. A schematic of the CVT reaction process is shown in Supporting

Information Figure S1. Nine metal halide transport agents were assessed for their ability to generate large crystals as well as a large quantity of crystals, as summarized in Supporting Information Table S1. Among the transport agents, CuCl_2 and FeCl_2 were found to be particularly effective at generating a large quantity of high-quality crystals as large as ~ 2 mm.

Preparation of Bulk HMS Samples. A large number of CVT reactions yielded sufficient crystalline material (~5 g) to be consolidated and pressed into bulk pucks by spark plasma sintering (SPS) for thermoelectric properties measurements. The HMS crystals were first hand-ground using a mortar and pestle into a fine powder and pressed under a pressure of 60 MPa for 5 min at a temperature of 950 °C, using a SPS 10-3 (Thermal Technology LLC).

Thermoelectric Properties Measurements. The resulting sample pucks were sectioned using a low-speed diamond saw and polished into parallelpipeds for properties measurements. The electrical conductivity σ (average sample dimensions of 1 \times 1 \times 6 mm) and Seebeck coefficient S (average sample dimensions of 3 \times 3 \times 0.5 mm) were measured in the temperature range of 10-823 K and 80-823 K, respectively, using a home-built and independently calibrated apparatus.³⁰ The thermal diffusivity, α_1 was measured on samples with dimensions of $6 \times 6 \times 1$ mm using a Netzsch LFA 457. The specific heat, C_p , was measured using a Netzsch 404 differential scanning calorimeter (DSC) using a sapphire reference, and the sample density, ρ , was measured by Archimedes' method. The total thermal conductivity, κ_{tot} was then calculated by $\kappa_{\text{tot}} = C_p \alpha \rho$. All transport properties were measured along the direction parallel to the SPS pressing force. The room temperature Hall coefficient measurements were performed using a Physical Properties Measurement System (PPMS, Quantum Design) with the magnetic field sweeping between ± 2 T. The resulting carrier concentration p and Hall mobility $\mu_{\rm H}$ were calculated by $p=-(1/{\rm e}R_{\rm H})$ and $\mu_{\rm H}=\sigma R_{\rm H}$, respectively. The percent uncertainty in the thermoelectric properties are as follows: electrical conductivity 5%, Seebeck coefficient 5%, thermal conductivity 7%, carrier concentration 6%, mobility 8%, and ZT 15%.

Structural Analysis. The samples were initially characterized by powder X-ray diffraction (PXRD) using a Siemens STOE diffractometer using Cu K α radiation ($\lambda = 1.5418$ Å). For high resolution powder X-ray diffraction (HRPXRD), finely ground samples with particle size < 40 μ m were packed into 0.6 mm quartz capillaries that were flame-sealed under a residual vacuum of $\sim 10^{-3}$ Torr. HRPXRD was performed using synchrotron radiation at Argonne National Laboratory on the Advanced Photon Source (APS), beamline 11-BM using a 12-analyzer Si detector and calibrated radiation wavelength of 0.412455 Å. 41,42 The capillaries were placed in a double-tilt goniometer in transmission geometry (Debye-Scherrer method) and rotated at ~500 rpm. A calibrated hot air blower (operational from room temperature to 1000 °C accurate to ±5 °C) was situated approximately 5 mm below the spinning capillary. The microstructure of finely polished samples was observed using a LEO Supra 55 VP field emission scanning electron microscope (SEM) with an electron backscatter detector (EBSD) operating at 10 kV. Transmission electron microscopy (TEM) of finely ground powder samples dispersed onto Cu TEM grids was performed using a FEI Titan aberration-corrected (S)TEM electron microscope operating at 200

■ RESULTS AND DISCUSSION

Crystal Growth Chemistry and Morphology. CVT is a well-known vapor—solid crystal growth process that enables the growth of high-quality crystals within a thermochemical potential. Typically, a transport agent is added to facilitate in vaporizing the transported species. The vaporized species migrate along a temperature gradient in the gaseous phase, nucleating as crystals at the hot zone (for an exothermic reaction) or cold zone (for an endothermic reaction). ⁴³ CVT has been used to grow single crystals and nanowires of metal silicides. ^{43–46} The HMS was synthesized by a modified CVT

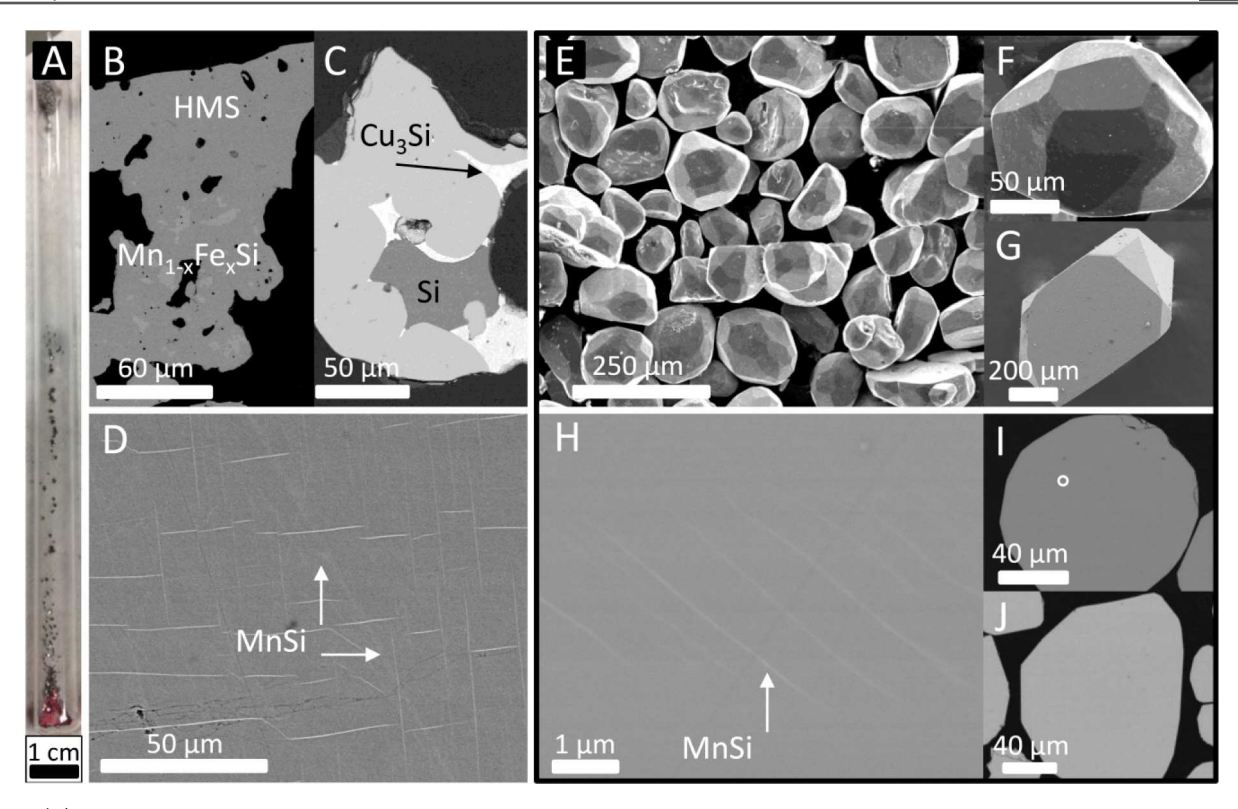


Figure 1. (A) Photograph of the sealed fused silica tube for HMS crystal growth using CuCl₂ as the transport agent, showing the starting material in the source zone (top, analysis on left side of figure) and product at the growth zone (bottom, analysis on right side of figure in dark box). The pink crystals in the growth zone are MnCl₂. (B) and (C) are SEM-EBSD micrographs of the source material following transport of the FeCl₂ (B) and CuCl₂ (C) CVT reactions, showing the Cu/Fe-rich phases incorporated. (D) is an SEM-EBSD micrograph of the source materials used in the study prepared by a solid-state reaction (SSR), showing an extended network of MnSi lamellae (light contrast features) throughout the HMS matrix. (E) shows the SEM images of the HMS single crystal products obtained by CVT, with detail of well-faceted crystals obtained using CuCl₂ (F) and FeCl₂ (G). (H) shows an SEM-EBSD micrograph of a very minor region of MnSi observed in a CVT crystal synthesized using CuCl₂ extending only a few micrometers within the observed crystal (I, region analyzed circled). No crystals grown using FeCl₂ exhibited observable MnSi precipitation (J).

approach that was originally reported by Kojima et al. as an effective means to generate HMS crystals as large as several millimeters in size. ^{38,39} We adapted this approach to prepare single crystalline, high purity HMS samples as well as to avoid the precipitation of MnSi within the crystals.

In the initial stages of our study, we explored a large number of metal halide transport agents to grow HMS crystals as summarized in Supporting Information Table S1. Of the transport agents investigated, we found that both FeCl₂ and CuCl₂ were most effective at producing a pure HMS product with good yield (~40–50% by mass). A typical CVT reaction tube following crystallization is shown in Figure 1A. Following the CVT growth using FeCl₂ and CuCl₂, the single crystal HMS products were mixed with pink crystals of MnCl₂ (bottom of Figure 1A), indicating that the chemical substitution of Mn within the source material helps to facilitate enhanced vaporization of the reactants during the process. Furthermore, analysis of the source untransferred material after the reaction reveals regions that clearly show the incorporation of the added Cu or Fe transition metals (Figure 1B,C).

For CuCl₂, a composite of Cu₃Si and Si were observed at the source (Figure 1C). Assuming total exchange of Cu/Mn, this implies the net reaction at the source proceeds as

$$\begin{aligned} & \text{MnSi}_{1.73}(s) + x \text{CuCl}_2(g) \\ & \rightarrow & \text{Mn}_{1-x} \text{Si}_{1.73-(x/3)}(s) + x \text{MnCl}_2(g) + x/3 \text{Cu}_3 \text{Si}(s) \end{aligned} \tag{1}$$

As for the excess Si, it is possible it comes from the dissociation of MnSi_{1.73} during the vaporization of HMS into a gaseous phase, i.e.,

$$MnSi_{1.73} \rightarrow MnSi + 0.73Si$$
 (2)

For FeCl₂, a mixture of MnSi_{1.73} and MnSi were observed doped with some amount of Fe (Figure 1B). Assuming total exchange of Fe/Mn and generation of a MnSi phase, this implies the net reaction at the source proceeds as

$$MnSi_{1.73}(s) + xFeCl_2(g)$$

$$\rightarrow Mn_{1-x-y}Si_{1.73-z}(s) + xMnCl_2(g) + Mn_yFe_xSi_z(s)$$
(3)

In each case, the substitution of the transition metal at the source side contributes to the generation of MnCl₂, which in turn enhances vapor transport of the HMS starting material. Interestingly, when we used MnCl₂ directly as a transport agent, the transport of the HMS was not as effective, resulting in low yield and very small crystals (Supporting Information Table S1). For many vapor and flux crystal growth reactions, frequently the growth media can become incorporated into the grown crystals. We therefore conducted inductively coupled plasma atomic emission spectroscopy (ICP-AES) analysis of the crystals dissolved in HF/HNO₃ to determine the concentration of Cu and Fe impurities present in the crystals relative to Mn concentration. In each case, the concentration of Cu and Fe in the crystals was essentially negligible (see Tables

S2, S3, S4 and S5 in the Supporting Information), indicating that the vaporization chemistry of the crystals was primarily dependent on the generation of MnCl₂ at the source from the reaction with Cu/FeCl₂, which then facilitated in enhanced crystal growth during the CVT process.

The well-faceted HMS crystals obtained exhibit a range of sizes with an average size of $100-200~\mu m$ (Figure 1E,F,G), with some crystals growing as large as a few millimeters in size. Single crystal cross sections analyzed by SEM-EBSD showed virtually no visible MnSi incorporation except for only a few crystals (Figure 1H,I,J). In those crystals, the incorporated MnSi was very minute, extending only for a few micrometers within the few crystals that had observable impurities. In contrast, for a sample prepared by a conventional solid-state reaction and used as the source material for the CVT reactions, the MnSi lamellae are much larger, forming interconnected networks extending hundreds of micrometers throughout the sample (Figure 1D). The MnSi lamellae were examined by SEM-EDS as shown in Figure S2 in the Supporting Information.

Verification of Purity of HMS Crystals by Synchrotron **HRPXRD.** To further verify the purity of the HMS crystals with respect to the incorporation of MnSi impurity inclusions, we conducted high-resolution PXRD (HRPXRD). Using synchrotron radiation, the extremely high (bright) flux of photons and short wavelength can afford a very sensitive measurement as directly compared to a typical laboratory PXRD instrument. The starting SSR source material (as described in the Experimental Section and SEM shown in Figure 1D) shows no detectable MnSi impurities when examined using a conventional Cu K α laboratory PXRD instrument; however, synchrotron HRPXRD clearly reveals the characteristic (110), (111), (210), and (211) reflections associated with the MnSi impurity phase at $2\theta = 27.7$, 34.1, 44.4, and 49.0° , respectively (Figure 2A). In comparing the SSR and CVT samples, the MnSi impurity peaks are clearly observed in the SSR sample but not for the HMS single crystal samples grown by CVT (Figure 2B and inset, MnSi reflections marked by asterisks). Additionally, in each sample a series of small reflections are observed around $2\theta = 45^{\circ}$ (as shown in the CuCl₂ and FeCl₂ CVT diffractograms in the inset of Figure 2B), which can be attributed to the $(0\ 2\ 2(m-n))$ and $(1\ 2\ (m+n))$ reflections that are typically obscured by lower-resolution analysis (see more details in Supporting Information Figure S3). These minor reflections can be differentiated from the brightest MnSi (210) reflection located at $2\theta = 44.4^{\circ}$ in the HRPXRD. However, the slight overlap of these peaks means we cannot conclusively say the samples are completely free of MnSi; indeed, SEM analysis (Figure 1H) reveals very minor MnSi in these samples that could be below the resolution limit of the synchrotron radiation used in this experiment.

Analysis of Phase Purity and Identification Using TEM. TEM of ground samples revealed no obvious MnSi impurities, likely arising from their extremely dilute nature. High resolution TEM images clearly showed the characteristic superstructure perpendicular to the c-axis of HMS along both the $\langle 110 \rangle$ and $\langle 120 \rangle$ directions (Figure 3A,B) whereas the view down the c-axis of the structure is observed along the $\langle 001 \rangle$ direction (Figure 3C). The existence of these features is well-documented for HMS, 20,47 arising from the structural complexity of the HMS crystal structures, i.e., the mismatch in the periodicity of the interpenetrated Mn and Si sublattices. This mismatch and the resulting electron diffraction patterns with

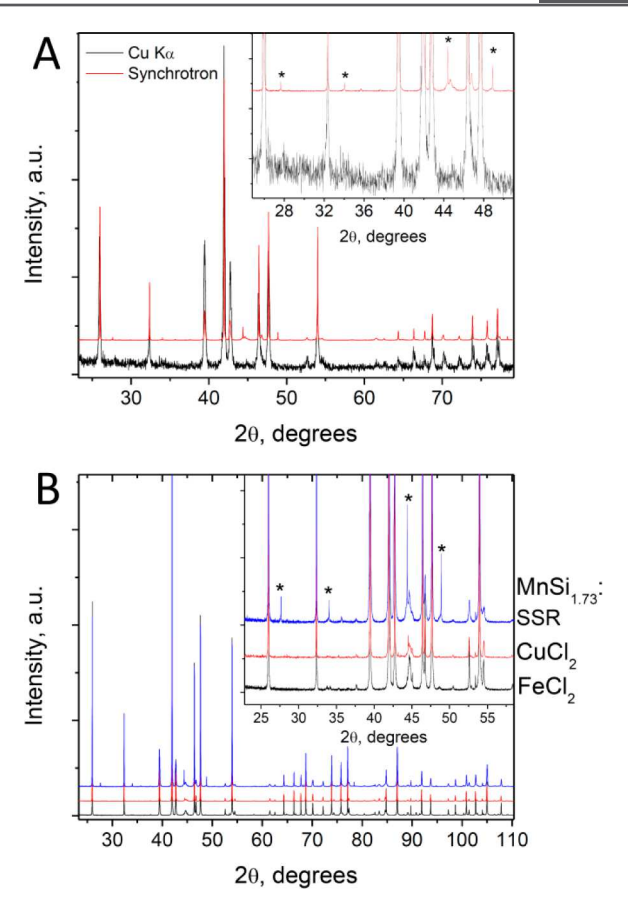


Figure 2. (A) Demonstration of the enhanced resolution and sensitivity of the synchrotron HRPXRD of the same HMS sample made by solid-state reaction (SSR) shown in Figure 1D. The high resolution of the synchrotron HRPXRD clearly shows MnSi, whereas the laboratory Cu $K\alpha$ source does not. (B) HRPXRD showing CVT samples synthesized using CuCl₂ and FeCl₂ as transport agents in comparison with the HMS prepared by SSR. Asterisks mark reflections associated with MnSi impurity.

satellite peaks (insets of Figure 3A,B) can be used to accurately identify the specific periodicity of the sublattices (i.e., the commensurability) and thus deduce the specific commensurate HMS phase. 20,47 We attempted analysis of these structures but were unable to determine a specific commensurate phase of HMS (see Figure S4 and additional discussion in the Supporting Information). Note that the indices used here are based on the Mn₄Si₇ phase, though the a and b indices do not significantly change across the homologous structures of HMS. It is likely that the CVT process does produce specific HMS phases as a result of this preparation; in fact, such analysis on HMS single crystals prepared by zone-refining, HMS prepared by solid-state synthesis, and also HMS nanostructures has shown a coexistence of several commensurate and incommensurate HMS phases. ^{20,22,37} Presumably, HMS synthesized in bulk-like quantities could contain a mixture of different HMS subphases that arise from local variability or inhomogeneity during the growth process. This can be especially exacerbated in the CVT system described here, where the temperature difference in the CVT tube in the growth zone (see Figure 1A) can differ by ~10-20 °C. We suspect that the very slight differences in the growth temperature and pressure could result in a mixture of HMS subphases, but at this point only incommensurate HMS phases have been observed.

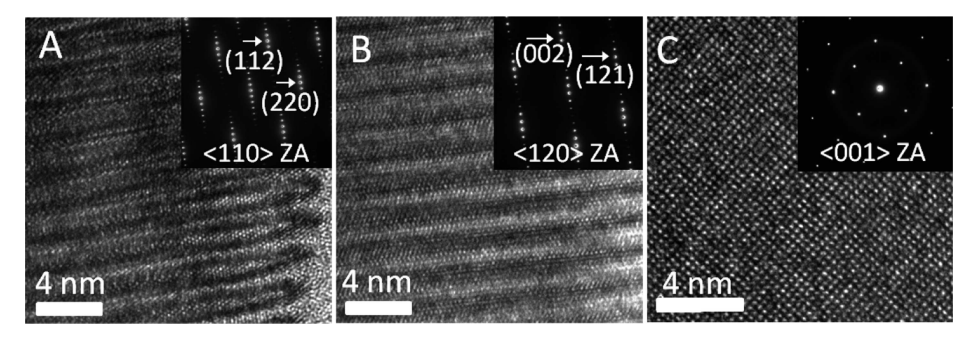


Figure 3. HRTEM analysis of HMS samples. Images taken along the (A) $\langle 110 \rangle$, (B) $\langle 120 \rangle$, and (C) $\langle 001 \rangle$ zone axes of an HMS crystal synthesized using FeCl₂ show characteristic microstructural features and electron diffraction (inset).

High-Temperature PXRD Stability Studies. To determine the stability of the high purity HMS crystals, we performed in situ high temperature synchrotron HRPXRD analysis of the crystals (Figure 4). In both the crystal samples grown using CuCl2 and FeCl2 transport agents, precipitation of MnSi is observed around 900 °C, as evidenced by the appearance of clearly defined MnSi reflections. Therefore, the inherent thermodynamic instability of the HMS phases at high temperature seem to make the appearance of MnSi impurity phase unavoidable either during high-temperature sample preparation (such as the SPS process used in this work) or for high temperature thermoelectric cycling. Similar effects have been observed previously in bulk HMS samples, 48,49 albeit using HMS samples prepared by arc melting where likely larger or more concentrated MnSi precipitates are readily observed using laboratory Cu K α PXRD instruments. The SEM-EBSD micrographs of the SPS-sintered samples reveal the precipitation of MnSi impurities in both CVT crystal samples (Figures 4B,C). Interestingly, the morphology of MnSi precipitates is different between the two samples. For the CuCl₂ CVT samples, the MnSi precipitates primarily at the grain boundaries between the HMS crystals as $1-5 \mu m$ round inclusions (Figure 4B). For FeCl₂ CVT samples (Figure 4C), the MnSi precipitates as the characteristic lamellae typically observed in HMS samples made by SSR (as shown in Figure 1D), but much smaller in size and more sparse in density.

Thermoelectric Properties. The thermoelectric properties of the HMS crystals grown by CVT and consolidated using SPS are compared with a SSR sample consolidated by SPS in the same manner²⁸ in Figure 5. It is important to note that the sample prepared by solid-state synthesis is not doped but has been prepared with a very slight excess of Si to minimize MnSi precipitation. This has been shown to help improve the thermoelectric performance in these samples, which is coupled with the optimized SPS procedure to produce a highly dense (i.e., >95%) sample. Therefore, the SSR sample shown in Figure 5 represents our highest-performing undoped HMS sample prepared under the most optimal synthetic conditions thus far. In directly comparing the samples, both CVT samples exhibit higher electrical conductivity over the entire temperature range, albeit very slightly, with an enhancement of ~50-70 S cm⁻¹ from the SSR to CVT samples (Figure 5A). The thermopower between samples is quite similar, with virtually no difference between the CVT samples (Figure 5B). To better ascertain the origins of the different electronic transport in these samples, we conducted Hall effect studies of the samples, to calculate the hole carrier concentration and hole mobilities. Assuming a single parabolic band, the hole concentration (n)was calculated from the Hall coefficient (R_H) assuming n = 1/2

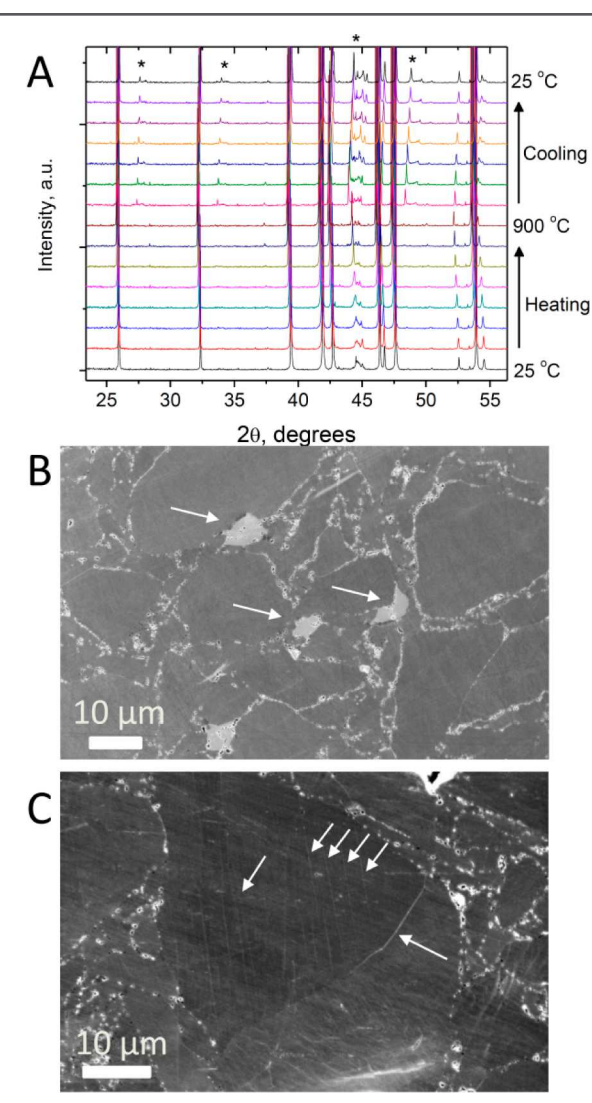


Figure 4. Analysis of phase stability of HMS crystals at high temperatures. (A) In situ high temperature studies of the CVT crystals reveal the appearance of peaks associated with of MnSi (shown by asterisks) after heating to 900 °C. (B) SEM microstructure of the CVT CuCl₂ crystals prepared by SPS, revealing large inclusions of MnSi have precipitated (arrows). (C) SEM microstructure of CVT FeCl₂ crystals prepared by SPS, revealing small MnSi lamellae have precipitated throughout the crystallites.

 $eR_{\rm H}$. The hole mobility was then determined from measured electrical conductivity σ , using $\sigma = ne\mu$, where $n = {\rm carrier}$ concentration, $e = {\rm fundamental}$ electron charge, and $\mu = {\rm hole}$

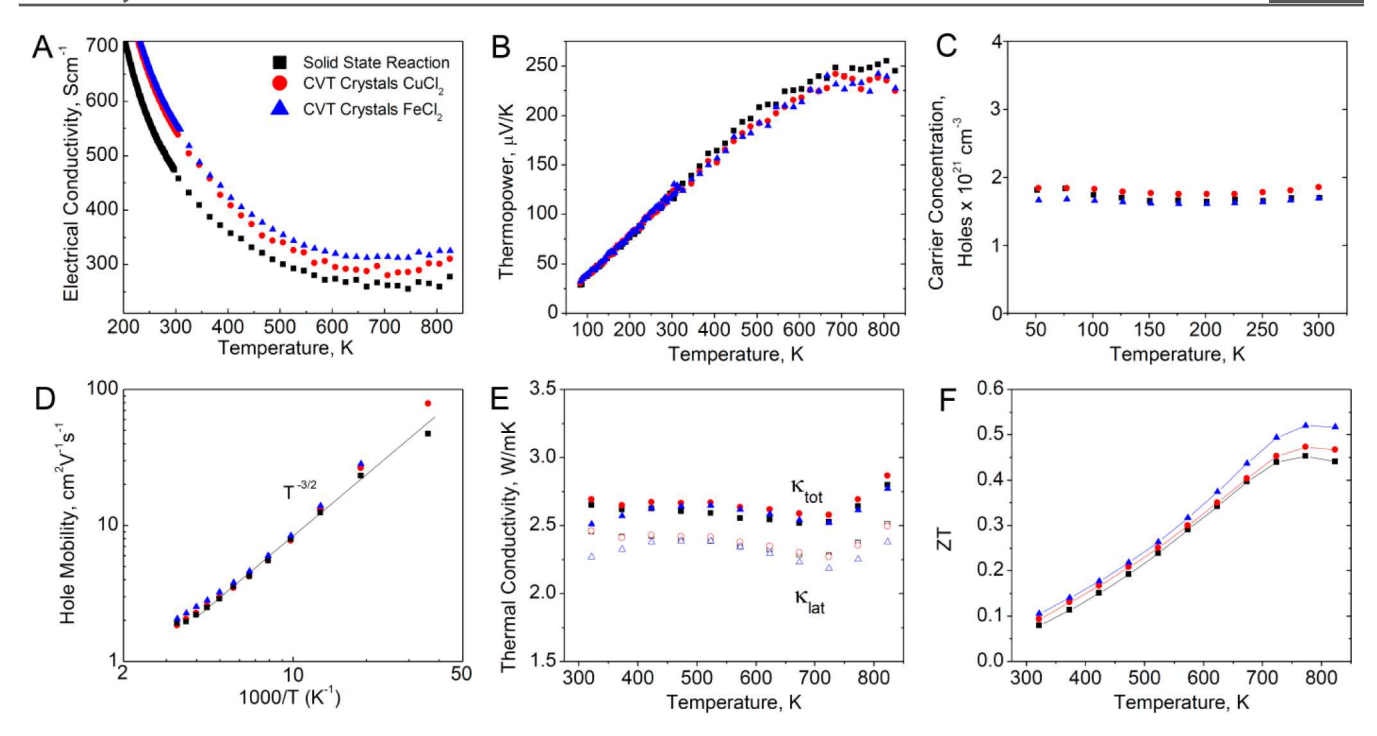


Figure 5. (A) Electrical conductivity, (B) thermopower, (C) hole concentration, (D) hole mobility, (E) total and lattice thermal conductivity (κ_{tot} and κ_{lat}), and (F) ZT of HMS made by SSR²⁸ and CVT. An enhancement in hole mobility produces a higher electrical conductivity in the CVT samples. The ZT of the CVT samples is slightly enhanced over the SSR sample, resulting from an enhancement in hole mobility.

mobility. The room-temperature physical properties of these three samples are listed in Supporting Information Table S6.

The carrier concentration data, shown in Figure 5C and Supporting Information Table S6, reveal that each sample has virtually the same hole concentration, between 1.54 and 1.81 × 10²¹ cm⁻³, reaffirming that the CVT growth of the crystals neither affects the doping by potential incorporation of Cu/Fe impurity atoms nor greatly distorts the electronic band structure of the HMS. However, the hole mobility data (Figure 5D) show that both CVT samples exhibit enhanced mobilities $(\sim 10-20\%$, above the 8% uncertainty in the measurement) over the entire temperature range. Because these samples are prepared in a similar manner with similar densities, the CVT samples show enhanced hole mobilities owing to their higher purity and likely fewer scattering sites. Furthermore, the very slight enhancement from the CuCl₂ to FeCl₂ CVT samples could arise from the different types of MnSi structures precipitated. Much previous work has been focused on the role of microstructures, and particularly nanostructures, on the electronic and thermal transport of thermoelectric materials. 50,51 Of note are recent studies investigating the role of coherent versus incoherent microstructures in thermoelectric composites; 52,53 in most cases, the smaller the size of the inclusion, the more accommodating the matrix to the associated strain, which aids in the formation of coherent boundaries. As the inclusion grows larger, the strain between the matrix and precipitate produces increased interfacial energy, causing incoherent boundaries to form. Incoherent grain boundaries are more effective in scattering carriers, reducing carrier mobility. Our findings here suggest that the larger MnSi inclusions formed within the CuCl₂ CVT samples produce more scattering centers arising from the incoherence between HMS matrix and MnSi particle caused by the larger size of the MnSi impurities generated. Conversely, the much smaller, more coherent lamellae-like MnSi precipitates formed in the HMS

sample made from the FeCl₂ CVT crystals exhibit fewer scattering sites and thus higher mobilities.

The total and lattice thermal conductivities are shown in Figure 5E. The specific heat and thermal diffusivity data are presented in Supporting Information Figure S5. The lattice thermal conductivities in the range of 300 to 850 K were calculated based on a two-band model following a prior work.³⁰ It can be seen that all samples have comparable values of thermal conductivity. The very small differences between samples are within the error range of the measurement. These results reveal that neither the SPS preparation nor the differences in the incorporated precipitates has any appreciable effect on the thermal transport. As a result, the obtained differences in ZT (Figure 5F) come exclusively from the mobility enhancements between the CVT synthesized samples and the SSR sample. Our findings here show that the higher purity of the CVT samples lends to a small enhancement of ZT over an optimized sample prepared by SSR, from values of 0.45 \pm 0.06 to 0.52 \pm 0.08 at 750 K. These samples exhibit some of the highest ZT for an undoped HMS material. Therefore, even though the appearance of MnSi impurity during high temperature processing of HMS samples is difficult to avoid, using high purity crystals of HMS in the preparation of these samples could enable the possibility to more finely control the MnSi precipitates and minimize the scattering centers, enhancing hole mobility and electrical conductivity. Furthermore, our findings suggest that the presence of metallic MnSi impurities as low concentrations, such as what is observed for HMS materials made from single crystals, affect only the hole mobility and electrical conductivity by the scattering of holes and have little effect on the electronic structure (i.e., doping or Seebeck coefficient) or phonon transport (i.e., thermal conductivity).

CONCLUSIONS

In summary, we report the synthesis, structural characterization, and thermoelectric properties of high-purity undoped HMS single crystals grown by chemical vapor transport (CVT) and bulk samples consolidated using spark plasma sintering (SPS). Despite the CVT crystals initially being free of MnSi impurities, thermodynamic instability at high temperature naturally causes the precipitation of dilute MnSi impurities at high temperature. For HMS single crystals grown using CuCl₂ transport agent, MnSi precipitates as larger particles ($\sim 1-5 \mu m$), whereas the samples grown using FeCl₂ exhibited smaller MnSi precipitates (<100 nm). The hole mobility of the HMS samples made from CVT crystals is enhanced over samples synthesized using traditional solid-state techniques. Our findings show that MnSi precipitation could be an unfortunate reality in virtually all bulk HMS TE materials. However, at low concentrations the MnSi precipitates affect only the electrical conductivity by producing hole scattering sites, with no observable effects to the carrier concentration or phonon transport. Owing to their improved mobilities, the higher-purity HMS samples synthesized from the CVT crystals produce slightly enhanced ZT, with a maximum of $\sim 0.52 \pm 0.08$ at 750 K.

ASSOCIATED CONTENT

S Supporting Information

Schematic of CVT reaction and images of CVT crystals, table of metal halide transport agents studied, ICP-AES analysis of CVT crystals, description of minor peaks observed in HRPXRD, and density, diffusivity, and specific heat measurements of the samples prepared by SPS. This material is available free of charge via the Internet at http://pubs.acs.org.

AUTHOR INFORMATION

Corresponding Author

*(S.J.) E-mail: jin@chem.wisc.edu.

Present Address

§(S.N.G.) Currently at University of Wisconsin—Whitewater.

Author Contributions

S.N.G. and S.J. devised the experiments. S.N.G. performed the material synthesis and characterized the phases by XRD and SEM. X.C. and J.Z. performed the SPS processing and thermoelectric properties measurements. S.N.G. and A.P. designed and performed the HRPXRD experiments. F.M. performed the TEM and analysis. All authors contributed to the writing of the paper.

Funding

The work was supported by NSF/DOE Joint Thermoelectric Partnership (NSF Award Numbers CBET-1048625 and CBET-1048767). S.N.G. gratefully acknowledges the NSF SEES Postdoctoral Fellowship for support (NSF Award Number EEC-1313968). Use of the Advanced Photon Source at Argonne National Laboratory was supported by the U.S. Department of Energy, Office of Science, Office of Basic Energy Sciences (Contract DE-AC02-06CH11357). The SPS processing and Hall measurements at the University of Texas at Austin were conducted with instruments acquired with the support of NSF Award Number DMR-1229131 and DMR-1122603.

Notes

The authors declare no competing financial interest.

REFERENCES

- (1) Bell, L. E. Science 2008, 321, 1457.
- (2) Sootsman, J. R.; Chung, D. Y.; Kanatzidis, M. G. Angew. Chem., Int. Ed. 2009, 48, 8616.
- (3) Szczech, J. R.; Higgins, J. M.; Jin, S. J. Mater. Chem. 2011, 21, 4037.
- (4) Snyder, G. J.; Toberer, E. S. Nat. Mater. 2008, 7, 105.
- (5) Biswas, K.; He, J.; Blum, I. D.; Wu, C.-I.; Hogan, T. P.; Seidman, D. N.; Dravid, V. P.; Kanatzidis, M. G. Nature 2012, 489, 414.
- (6) Heremans, J. P.; Jovovic, V.; Toberer, E. S.; Saramat, A.; Kurosaki, K.; Charoenphakdee, A.; Yamanaka, S.; Snyder, G. J. Science 2008, 321, 554.
- (7) Girard, S. N.; He, J.; Zhou, X.; Shoemaker, D.; Jaworski, C. M.; Uher, C.; Dravid, V. P.; Heremans, J. P.; Kanatzidis, M. G. *J. Am. Chem. Soc.* **2011**, *133*, 16588.
- (8) Yu, B.; Zebarjadi, M.; Wang, H.; Lukas, K.; Wang, H.; Wang, D.; Opeil, C.; Dresselhaus, M.; Chen, G.; Ren, Z. *Nano Lett.* **2012**, *12*, 2077
- (9) Zebarjadi, M.; Joshi, G.; Zhu, G.; Yu, B.; Minnich, A.; Lan, Y.; Wang, X.; Dresselhaus, M.; Ren, Z.; Chen, G. *Nano Lett.* **2011**, *11*, 2225
- (10) Zhou, X.; Wang, G.; Zhang, L.; Chi, H.; Su, X.; Sakamoto, J.; Uher, C. J. Mater. Chem. **2012**, 22, 2958.
- (11) Schmitt, A. L.; Higgins, J. M.; Szczech, J. R.; Jin, S. J. Mater. Chem. 2010, 20, 223.
- (12) Szczech, J. R.; Jin, S. J. Solid State Chem. 2008, 181, 1565.
- (13) Pandey, T.; Singh, D. J.; Parker, D.; Singh, A. K. J. Appl. Phys. **2013**, 114, 153704.
- (14) Zhou, F.; Szczech, J.; Pettes, M. T.; Moore, A. L.; Jin, S.; Shi, L. Nano Lett. 2007, 7, 1649.
- (15) Levinson, L. M. J. Solid State Chem. 1973, 6, 126.
- (16) Ivanenko, L.; Shaposhnikov, V. L.; Filonov, A. B.; Migas, D. B.; Behr, G.; Schumann, J.; Vinzelberg, H.; Borisenko, V. E. *Microelectron. Eng.* **2002**, *64*, 225.
- (17) Borisenko, V. E. Semiconducting Silicides; Springer: Berlin, 2000; Vol. 39.
- (18) Fedorov, M. I.; Zaitsev, V. K. In *CRC Handbook of Thermoelectrics*; Rowe, D. M., Ed.; Taylor & Francis Group, LLC: Boca Raton, 2006; p 31.
- (19) Flieher, G.; Voellenkle, H.; Nowotny, H. *Monatsh. Chem.* **1967**, 98, 2173.
- (20) Higgins, J. M.; Schmitt, A. L.; Guzei, I. A.; Jin, S. J. Am. Chem. Soc. 2008, 130, 16086.
- (21) De Ridder, R.; Van Tendeloo, G.; Amelinckx, S. Phys. Status Solidi A 1975, 30, K99.
- (22) De Ridder, R.; Amelinckx, S. Mater. Res. Bull. 1971, 6, 1223.
- (23) Itoh, T.; Yamada, M. J. Electron. Mater. 2009, 38, 925.
- (24) Norouzzadeh, P.; Zamanipour, Z.; Krasinski, J. S.; Vashaee, D. J. Appl. Phys. **2012**, 112, 124308.
- (25) Zhou, A. J.; Zhao, X. B.; Zhu, T. J.; Yang, S. H.; Dasgupta, T.; Stiewe, C.; Hassdorf, R.; Mueller, E. *Mater. Chem. Phys.* **2010**, *124*, 1001
- (26) Ponnambalam, V.; Morelli, D. J. Electron. Mater. 2011, 41, 1389.
- (27) Hou, Q. R.; Zhao, W.; Chen, Y. B.; Liang, D.; Feng, X.; Zhang, H. Y.; He, Y. *J. Appl. Phys. A* **200**7, *86*, 385.
- (28) Chen, X.; Girard, S. N.; Meng, F.; Lara-Curzio, E.; Jin, S.; Goodenough, J. B.; Zhou, J.; Shi, L. *Adv. Energy Mater.* **2014**, DOI: 10.1002/aenm.201400452.
- (29) Luo, W.; Li, H.; Fu, F.; Hao, W.; Tang, X. J. Electron. Mater. 2011, 40, 1233.
- (30) Chen, X.; Weathers, A.; Salta, D.; Zhang, L.; Zhou, J.; Goodenough, J. B.; Shi, L. J. Appl. Phys. 2013, 114, 173705.
- (31) Sadia, Y.; Gelbstein, Y. J. Electron. Mater. 2012, 41, 1504.
- (32) Hou, Q. R.; Gu, B. F.; Chen, Y. B.; He, Y. J. Phys. Status Solidi A 2012, 209, 1307.
- (33) Luo, W.; Li, H.; Yan, Y.; Lin, Z.; Tang, X.; Zhang, Q.; Uher, C. Intermetallics 2011, 19, 404.

(34) Aoyama, I.; Fedorov, M. I.; Zaitsev, V. K.; Solomkin, F. Y.; Eremin, I. S.; Samunin, A. Y.; Mukoujima, M.; Sano, S.; Tsuji, T. *Jpn. J. Appl. Phys.* **2005**, *44*, 8562.

- (35) Muehlbauer, S.; Binz, B.; Jonietz, F.; Pfleiderer, C.; Rosch, A.; Neubauer, A.; Georgii, R.; Boeni, P. Science 2009, 323, 915.
- (36) Du, H.; DeGrave, J. P.; Xue, F.; Liang, D.; Ning, W.; Yang, J.; Tian, M.; Zhang, Y.; Jin, S. Nano Lett. **2014**, *14*, 2026.
- (37) Pokhrel, A.; Degregorio, Z. P.; Higgins, J. M.; Girard, S. N.; Jin, S. Chem. Mater. 2013, 25, 632.
- (38) Kojima, T.; Nishida, I.; Sakata, T. J. Cryst. Growth 1979, 47, 589.
- (39) Kojima, T.; Nishida, I. Jpn. J. Appl. Phys. 1975, 14, 141.
- (40) Shukla, A.; Kang, Y.-B.; Pelton, A. D. Calphad 2008, 32, 470.
- (41) Lee, P. L.; Shu, D.; Ramanathan, M.; Preissner, C.; Wang, J.; Beno, M. A.; Von Dreele, R. B.; Ribaud, L.; Kurtz, C.; Antao, S. M.; Jiao, X.; Toby, B. H. *J. Synchrotron Radiat.* **2008**, *15*, 427.
- (42) Wang, J.; Toby, B. H.; Lee, P. L.; Ribaud, L.; Antao, S. M.; Kurtz, C.; Ramanathan, M.; Dreele, R. B. V.; Beno, M. A. Rev. Sci. Instrum. 2008, 79, 085105.
- (43) Gruehn, R.; Glaum, R. Angew. Chem., Int. Ed. 2000, 39, 692.
- (44) Szczech, J. R.; Schmitt, A. L.; Bierman, M. J.; Jin, S. Chem. Mater. 2007, 19, 3238.
- (45) Szczech, J. R.; Jin, S. J. Mater. Chem. 2010, 20, 1375.
- (46) Song, Y.; Schmitt, A. L.; Jin, S. Nano Lett. 2007, 7, 965.
- (47) Ye, H. Q.; Amelinckx, S. J. Solid State Chem. 1986, 61, 8.
- (48) Allam, A.; Nunes, C. A.; Zalesak, J.; Record, M.-C. J. Alloy. Compd. 2012, 512, 278.
- (49) Allam, A.; Boulet, P.; Nunes, C. A.; Sopousek, J.; Broz, P.; Record, M. C. J. Alloy. Compd. 2013, 551, 30.
- (50) Girard, S. N.; Schmidt-Rohr, K.; Chasapis, T. C.; Hatzikraniotis, E.; Njegic, B.; Levin, E. M.; Rawal, A.; Paraskevopoulos, K. M.; Kanatzidis, M. G. *Adv. Funct. Mater.* **2013**, 23, 747.
- (51) Girard, S. N.; Chasapis, T. C.; He, J.; Zhou, X.; Hatzikraniotis, E.; Uher, C.; Paraskevopoulos, K. M.; Dravid, V. P.; Kanatzidis, M. G. *Energy Environ. Sci.* **2012**, *5*, 8716.
- (52) He, J.; Blum, I. D.; Wang, H.-Q.; Girard, S. N.; Doak, J.; Zhao, L.-D.; Zheng, J.-C.; Casillas, G.; Wolverton, C.; Jose-Yacaman, M.; Seidman, D. N.; Kanatzidis, M. G.; Dravid, V. P. *Nano Lett.* **2012**, *12*, 5979
- (53) He, J.; Girard, S. N.; Kanatzidis, M. G.; Dravid, V. P. Adv. Funct. Mater. **2010**, 20, 764.